

Weak Boundary Conditions for Lagrangian Shock Hydrodynamics: A High-Order Finite Element Implementation on Curved Boundaries

Nabil M. Atallah^{a,*}, Vladimir Z. Tomov^a, Guglielmo Scovazzi^b

^a*Lawrence Livermore National Laboratory, Livermore (CA), USA*

^b*Department of Civil and Environmental Engineering, Duke University, Durham, North Carolina 27708, USA*

Abstract

We propose a new Nitsche-type approach for weak enforcement of normal velocity boundary conditions for a Lagrangian discretization of the compressible shock-hydrodynamics equations using high-order finite elements on curved boundaries. Specifically, the variational formulation is appropriately modified to enforce free-slip wall boundary conditions, without perturbing the structure of the function spaces used to represent the solution, with a considerable simplification with respect to traditional approaches. Total energy is conserved and the resulting mass matrices are constant in time. The robustness and accuracy of the proposed method are validated with an extensive set of tests involving nontrivial curved boundaries.

Keywords: Lagrangian hydrodynamics; wall boundary conditions; curved boundaries; high-order finite elements.

1. Introduction

This work is motivated by the need to perform Lagrangian hydrodynamics simulations in domains with non-trivial and possibly curved boundaries. The most common boundary condition (BC) in simulations of Lagrangian shock hydrodynamics is the free-slip wall BC, $\mathbf{v} \cdot \mathbf{n} = 0$, where the fluid particles are allowed to slip tangentially along the wall's surface. Correct enforcement of these conditions is essential for accurately modeling and simulating fluid behavior in confined geometries, such as containers or channels, or when the flow must go around internal obstacles. A few approaches have been proposed in the past for incompressible flows [6, 11], but, to the best of our knowledge, there is no method that enforces wall BC robustly for high-order FE Lagrangian simulations of compressible flows in general curved geometries.

The starting point of this work is the high-order Finite Element (FE) method of Dobrev *et al.* [10] (open-source version available at [14]). This method has proven itself over the years, demonstrating high-order accuracy, robust behavior for various problems, good symmetry preservation, accurate capturing of the flow geometry; the method has been used as a backbone of a next-generation multiphysics simulation code [3]. However, a major restriction of the original formulation is that it is only applicable to straight boundaries, i.e., when the boundary normals \mathbf{n} are parallel to one of the coordinate axes. This limitation is not just specific to the algorithms described in [3, 10, 14], but to vast majority of the high-order Lagrangian and Arbitrary Lagrangian-Eulerian (ALE) shock-hydrodynamic codes in the literature [1, 9, 12, 15, 19].

Enforcing wall BC on general boundaries with FE can be done by strong enforcement, i.e., by posing constraints on the linear system level, or by weak enforcement, i.e., by adding certain penalty force integrals in the variational formulation. While strong enforcement is generally more accurate, it becomes complex when the different velocity components need to couple, and requires manipulations in the linear algebra operators. Weak

*Corresponding author: Nabil M. Atallah

Email addresses: atallah1@llnl.gov (Nabil M. Atallah), tomov2@llnl.gov (Vladimir Z. Tomov),
guglielmo.scovazzi@duke.edu (Guglielmo Scovazzi)

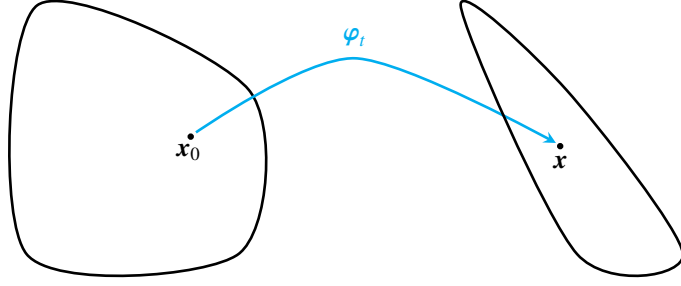


Figure 1: Sketch of the Lagrangian map φ_t .

enforcement, on the other hand, provides more flexibility as it allows unified treatment of different cases. Furthermore, enforcing the wall BC weakly through penalty integrals allows the use of numerical techniques like partial assembly and matrix-free computations, which enable high performance on the latest computer architectures [13, 27]. For these reasons, the focus of this work is weak enforcement.

We propose a new Nitsche-type approach for weak enforcement of free-slip wall boundary conditions. Nitsche's method [18] has been traditionally applied for the imposition of boundary conditions to elliptic and parabolic Partial Differential Equations (PDEs), and only more recently has been considered in the context of hyperbolic systems of PDEs [22, 25, 26], associated with acoustics, waves in solids, and shallow water flows. Our method is inspired by the developments in [25, 26], but aims at tackling the complex challenges associated with the strong nonlinearities of shock hydrodynamics, and introduces some important new ideas. The variational form of the momentum equation is enhanced by two penalty terms, affecting the mass matrix and the right-hand side, respectively. These terms are chosen in a way that the mass matrix stays constant in time. The variational form of the specific internal energy is adjusted in a similar manner, incorporating terms to ensure the preservation of total energy.

This article is organized as follows: Section 2 introduces the equations of Lagrangian shock hydrodynamics; Section 3 describes the principles and implementation of weak slip wall boundary conditions; Section 4 present a suite of numerical experiments; and Section 5 summarizes the conclusions and future work.

2. General equations of Lagrangian shock hydrodynamics

The classical equations of Lagrangian shock hydrodynamics govern the rate of change in position, momentum and energy of a compressible body of fluid, as it deforms. Let Ω_0 and Ω be open sets in \mathbb{R}^d (where d is the number of spatial dimensions.) The *motion*

$$\varphi_t : \Omega_0 \rightarrow \Omega = \varphi_t(\Omega_0) , \quad (1a)$$

$$\mathbf{x}_0 \mapsto \mathbf{x} = \varphi_t(\mathbf{x}_0) , \quad \forall \mathbf{x}_0 \in \Omega_0, t \geq 0 , \quad (1b)$$

maps the material coordinate \mathbf{x}_0 , representing the initial position of an infinitesimal material particle of the body, to \mathbf{x} , the position of that particle in the current configuration (see Fig. 1). Here Ω_0 is the domain occupied by the body in its initial configuration, with boundary $\partial\Omega_0 = \Gamma_0$ and outward-pointing boundary normal \mathbf{n}_0 . The transformation φ_t maps Ω_0 to Ω , the domain occupied by the body in its current configuration, with boundary $\partial\Omega = \Gamma$ and outward-pointing boundary normal \mathbf{n} . Usually φ_t is a *smooth*, invertible map, and the *deformation gradient* $\mathbf{F} = \nabla_{\mathbf{x}_0} \varphi_t$ and *deformation Jacobian determinant* $J = J(\mathbf{x}_0, t) := \det(\mathbf{F})$ can be defined by means of the original configuration gradient $\nabla_{\mathbf{x}_0}$.

In the domain Ω , we utilize the non-conservative form of the Euler system [7] and evolve the material position, density, velocity, and specific internal energy:

$$\dot{\mathbf{x}} = \mathbf{v} , \quad (2a)$$

$$\rho J = \rho_0 , \quad (2b)$$

$$\rho \dot{\mathbf{v}} = \rho \mathbf{b} + \nabla_x \cdot \boldsymbol{\sigma} , \quad (2c)$$

$$\rho \dot{e} = \rho r + \nabla_x \mathbf{v} : \boldsymbol{\sigma} - \nabla_x \cdot \mathbf{q} . \quad (2d)$$

Here ∇_x and $\nabla_x \cdot$ are the current configuration gradient and divergence operators, respectively, and $(\dot{\cdot})$ indicates the material, or Lagrangian, time derivative. Furthermore ρ_0 is the reference (initial) density with $\rho_{\max} := \sup_{x_0 \in \Omega_0} \rho_0(x_0) < \infty$, ρ is the (current) density, \mathbf{v} is the velocity, \mathbf{b} is the body force (e.g., gravity), $\boldsymbol{\sigma}$ is the symmetric Cauchy stress tensor, r is the energy source term, and \mathbf{q} is the heat flux. Using index notation, $\boldsymbol{\sigma}^T : \nabla_x \mathbf{v} = \sigma_{ji} \partial_x v_j$, and $\nabla_x \mathbf{v} : \boldsymbol{\sigma} = \boldsymbol{\sigma} : \nabla_x \mathbf{v} = \boldsymbol{\sigma}^T : \nabla_x \mathbf{v}$, since $\boldsymbol{\sigma}$ is symmetric. We also denote by $E = e + \mathbf{v} \cdot \mathbf{v}/2$ the total energy per unit mass, the sum of the specific internal energy e and the kinetic energy $\mathbf{v} \cdot \mathbf{v}/2$. Obviously, E, e, \mathbf{b}, r are measured per unit mass.

The system of equations (2) are most commonly adopted in shock-hydrodynamics algorithms [7] and make use of the quasi-linear rather than the conservative form of the internal energy equation. The sum of the internal energy equation (2d) and the kinetic energy equation (the product of (2c) by the velocity vector \mathbf{v}) yields the equation for the conservation of total energy.

The system of equations (2) completely defines the evolution of the system, once constitutive relationships for the stress $\boldsymbol{\sigma}$ and heat flux \mathbf{q} are specified, together with appropriate initial and boundary conditions.

2.1. Constitutive laws

For a compressible inviscid fluid, the Cauchy stress $\boldsymbol{\sigma}$ reduces to an isotropic tensor, dependent only on the thermodynamic pressure, namely

$$\boldsymbol{\sigma} = -p \mathbf{I}_{d \times d} + \boldsymbol{\sigma}' , \quad (3)$$

where an equation of state of the type

$$p = \mathcal{P}(\rho, e) , \quad (4)$$

is assumed. The deviatoric stress $\boldsymbol{\sigma}'$ is calculated from either a hypoelastic or hyperelastic constitutive model. Mie-Grüneisen equations of state are of the form (4) with $\mathcal{P}(\rho, e) = f_1(\rho) + f_2(\rho)e$, and apply to materials such as compressible ideal gases, co-volume gases, high explosives, etc. (see [17] for more details). Ideal gases satisfy a Mie-Grüneisen equation of state with $f_1 = 0$ and $f_2 = (\gamma - 1)\rho$, namely

$$\mathcal{P}(\rho, e) = (\gamma - 1)\rho e , \quad (5)$$

where γ is the exponent of the isentropic transformation of the gas. Consequently, the sound speed c_s takes the form

$$c_s = \sqrt{\gamma(\gamma - 1)e} . \quad (6)$$

2.2. Boundary conditions

We assume that *slip boundary conditions* are enforced on the entire boundary Γ given as

$$\mathbf{v} \cdot \mathbf{n}_\Gamma = 0 , \quad (7a)$$

$$\boldsymbol{\tau}_i \cdot (\boldsymbol{\sigma} \mathbf{n}_\Gamma) = 0 , \quad (7b)$$

where \mathbf{n}_Γ is the outward-pointing normal to Γ . In particular (7a) and (7b) enforce that the normal component of the velocity and the tangential component of the distributed traction force must vanish at the wall.

2.3. General notation: Inner products, boundary functionals and norms

Throughout the paper, we will denote by

$$(\mathbf{v}, \mathbf{w})_\omega = \int_\omega \mathbf{v} \cdot \mathbf{w} \, d\omega \quad \text{and} \quad (\mathbf{v}, \mathbf{w})_\omega = \int_\omega \mathbf{v} \cdot \mathbf{w} \, d\omega \quad (8)$$

the $L^2(\omega)$ and the $(L^2(\omega))^d$ inner products on the interior of the domain $\omega \subset \Omega$, and by

$$\langle v, w \rangle_\gamma = \int_\gamma v w \, d\gamma \quad \text{and} \quad \langle \mathbf{v}, \mathbf{w} \rangle_\gamma = \int_\gamma \mathbf{v} \cdot \mathbf{w} \, d\gamma \quad (9)$$

a boundary functional on $\gamma \subset \Gamma$.

Let $L^2(\Omega)$ be the space of square integrable functions on Ω . We will use the Sobolev spaces $H^m(\Omega) = W^{m,2}(\Omega)$ of index of regularity $m \geq 0$ (where $H^0(\Omega) = L^2(\Omega)$), equipped with the (scaled) norm

$$\|v\|_{H^m(\Omega)} = \left(\|v\|_{L^2(\Omega)}^2 + \sum_{k=1}^m \|l(\Omega)^k \mathbf{D}^k v\|_{L^2(\Omega)}^2 \right)^{1/2}, \quad (10)$$

where \mathbf{D}^k is the k th-order spatial derivative operator and $l(A) = \text{meas}_d(A)^{1/d}$ is a characteristic length of the domain A with $\text{meas}(A)$ the Lebesgue measure of the set A . As usual, we use a simplified notation for norms and semi-norms, i.e., we set $\|v\|_{m,\Omega} = \|v\|_{H^m(\Omega)}$ and $|v|_{k,\Omega} = \|\mathbf{D}^k v\|_{0,\Omega} = \|\mathbf{D}^k v\|_{L^2(\Omega)}$.

3. A Nitsche approach to boundary conditions

Let \mathcal{T}^h be a family of admissible and shape-regular triangulations of Ω . We will denote by h_T the circumscribed diameter of an element $T \in \mathcal{T}^h$ and by h the piecewise constant function in Ω such that $h|_T = h_T$ for all $T \in \mathcal{T}^h$.

3.1. Discrete approximation spaces for the kinematic and thermodynamic variables

We rely on a semi-discrete formulation to derive the Nitsche weak variational formulation of the Euler equations in the Lagrangian reference frame for (2a)- (2d). The discretization is determined by two finite dimensional functional spaces on the initial domain Ω_0 :

- $\mathcal{V}(\Omega_0) \subset (H^1(\Omega_0))^d$: the discrete space for the kinematic variables, with basis $\{w_a\}_{a=1}^{n_\mathcal{V}}$.
- $\mathcal{E}(\Omega_0) \subset L_2(\Omega_0)$: the discrete space for the thermodynamic variables, with basis $\{\phi_l\}_{l=1}^{n_\mathcal{E}}$.

Note that we can define Lagrangian (moving) extensions of the kinematic and thermodynamic basis functions on $\Omega(t)$ through the formulas $w_a(\mathbf{x}, t) := w_a \circ \boldsymbol{\varphi}_t^{-1}(\mathbf{x}) = w_a(\mathbf{x}_0)$ and $\phi_l(\mathbf{x}, t) := \phi_l \circ \boldsymbol{\varphi}_t^{-1}(\mathbf{x}) = \phi_l(\mathbf{x}_0)$, for $1 \leq a \leq n_\mathcal{V}$ and $1 \leq l \leq n_\mathcal{E}$, respectively. These moving bases are constant along particle trajectories and therefore have zero material derivatives, that is,

$$\dot{w}_a = 0 \quad \text{and} \quad \dot{\phi}_l = 0. \quad (12)$$

The spaces associated with the deformed domain $\Omega(t)$ will be denoted by $\mathcal{V}(\Omega(t))$ and $\mathcal{E}(\Omega(t))$, respectively. A mild restriction on the space $\mathcal{V}(\Omega(t))$ is the requirement that

$$\mathbf{x}(\mathbf{x}_0, t_0) = \mathbf{x}_0, \quad \forall \mathbf{x}_0 \in \Omega_0, \quad (13)$$

expressing that we can represent exactly the initial geometry. We discretize the position $\mathbf{x}(t)$ of the particle \mathbf{x}_0 at time t using the expansion

$$\mathbf{x}(\mathbf{x}_0, t) := \boldsymbol{\varphi}_t(\mathbf{x}_0) = x_{i;a}(t) w_a(\mathbf{x}_0) \boldsymbol{\zeta}_i, \quad (14)$$

where $x_{i;a}(t)$ is the time-dependent, i th coordinate of the position unknown of index a and $\boldsymbol{\zeta}_i$ is the unit vector in the direction i , for $1 \leq i \leq d$. The discrete velocity field corresponding to the motion (14) is given by

$$\mathbf{v}(\mathbf{x}_0, t) := \dot{\boldsymbol{\varphi}}_t(\mathbf{x}_0) = v_{i;a}(t) w_a(\mathbf{x}_0) \boldsymbol{\zeta}_i, \quad (15)$$

where $v_{i;a}(t) = \dot{x}_{i;a}(t)$. Note that we can also think of the velocity as a function on $\Omega(t)$ with the expansion

$$\mathbf{v}(\mathbf{x}, t) = v_{i;a}(t) w_a(\mathbf{x}, t) \zeta_i.$$

Using the same coordinates, but in the moving kinematic basis. The thermodynamic discretization starts with the expansion of the internal energy in the basis $\{\phi_l\}_{l=1}^{n_\mathcal{E}}$:

$$e(\mathbf{x}_0, t) = e_l(t) \phi_l(\mathbf{x}_0). \quad (16)$$

Also the internal energy can also be expressed in the moving thermodynamic basis: $e(\mathbf{x}, t) = e_l(t) \phi_l(\mathbf{x}, t)$.

3.2. Semi-discrete mass conservation law

Given an initial density field $\rho_0(\mathbf{x}_0) = \rho(\mathbf{x}_0, t_0)$, we use the strong mass conservation principle (2b) to define the density pointwise at any time t ,

$$\rho(\mathbf{x}_0, t) = \frac{\rho_0(\mathbf{x}_0)}{J(\mathbf{x}_0, t)}, \quad (17)$$

which implies that the mass in every Lagrangian volume is preserved exactly.

3.3. Semi-discrete momentum conservation law

We formulate the discrete momentum conservation equation by applying a Galerkin variational formulation to the continuous equation (2c). At any given time t , we multiply (2c) by a moving test function basis $\{\mathbf{w}_{i;a}\}_{a=1}^{n_\mathcal{V}}$ constructed as $\mathbf{w}_{i;a} = w_a \zeta_i$, where $w_a \in \mathcal{V}(\Omega(t))$.

Integrating by parts over $\Omega(t)$ and enforcing continuity of the stress $\boldsymbol{\sigma}$ across internal faces and (7b) on $\Gamma(t)$, we obtain

$$(\rho \dot{\mathbf{v}}, \mathbf{w}_{i;a})_{\Omega(t)} + (\boldsymbol{\sigma}, \nabla_{\mathbf{x}} \mathbf{w}_{i;a})_{\Omega(t)} - \langle \mathbf{n} \cdot (\boldsymbol{\sigma} \mathbf{n}), \mathbf{w}_{i;a} \rangle_{\Gamma(t)} - (\rho \mathbf{b}, \mathbf{w}_{i;a})_{\Omega(t)} = 0. \quad (18)$$

Unlike [10], the boundary integral term will not vanish since (7a) is not embedded in the function space $\mathcal{V}(\Omega(t))$. Expanding the velocity in terms of the moving velocity basis, observing that $\zeta_i \cdot \zeta_j = \delta_{ij}$ (the Kronecker delta tensor) and $b_i := \mathbf{b} \cdot \zeta_i$, and using index notation give us

$$(\rho \dot{v}_{i;b}(t) w_b, w_a)_{\Omega(t)} + (\sigma_{ik}, \nabla_{x_k} w_a)_{\Omega(t)} - \langle (n_k \sigma_{kj} n_j) n_i, w_a \rangle_{\Gamma(t)} - (\rho b_i, w_a)_{\Omega(t)} = 0. \quad (19)$$

We proceed now to the weak enforcement of (7a), by adding two penalty terms to (18) (or (19)). The first term is

$$\langle \beta \rho c_s \mathbf{v} \cdot \mathbf{n}, w_a \mathbf{n} \cdot \zeta_i \rangle_{\Gamma(t)} = \langle \beta \rho c_s v_k n_k, w_a n_i \rangle_{\Gamma(t)}, \quad (20)$$

which specifically enforces the slip boundary condition (7a). Here $\beta = 20 C_I$ is a non-dimensional constant, while the choice of ρc_s is standard to ensure the term has the correct units. Following [29], the penalty scale is chosen to increase with the increase of the polynomial degree:

$$C_I = \begin{cases} (k+1)(k+d)d^{-1} & \text{for simplices in } d \text{ dimensions} \\ (k+1)^2 & \text{for quadrilaterals and hexahedra,} \end{cases} \quad (21)$$

where k is the order of the spatial polynomial discretization for the velocity. The second penalty term is

$$\langle \alpha_0 \rho_{\max} L \dot{\mathbf{v}} \cdot \mathbf{n}_0, w_a \mathbf{n}_0 \cdot \zeta_i \rangle_{\Gamma_0} = \dot{v}_{j;b} \langle \alpha_0 \rho_{\max} L w_b n_{0;j}, w_a n_{0;i} \rangle_{\Gamma_0}, \quad (22)$$

which enforces the condition $\dot{\mathbf{v}}(\mathbf{x}_0, t) \cdot \mathbf{n}_0(\mathbf{x}_0) = 0$, that is, that the acceleration in the initial configuration frame is orthogonal to the boundary normal in the initial configuration. This condition is equivalent to $d/dt(\mathbf{v} \cdot \mathbf{n}) = 0$ for boundary surfaces that do not move in the normal direction, like the ones considered in this work. In this case, \mathbf{n} stays constant over time and in particular $\mathbf{n}_0 = \mathbf{n}$, so that $d/dt(\mathbf{v} \cdot \mathbf{n}) = \dot{\mathbf{v}} \cdot \mathbf{n}_0$. In (22), L is the perimeter (unit of length) of the bounding box of Ω_0 , $\alpha_0 = \beta L / J_{\square}^{1/d}$ is a non-dimensional constant, and $J_{\square} = \det(\mathbf{F}_{\square})$ with $\mathbf{F}_{\square} = \nabla_{\xi} \mathbf{X}$ is the deformation gradient of the mapping from the parent domain to the original configuration. In

choosing the scaling in (22), the two key points are dimensional consistency and time-independence. Hence, a natural choice would be $\beta \rho_{\max} L$. However, multiplying the latter scaling by the dimensionless ratio $L/J_{\square}^{1/d}$ is critical to ensure that (22) does not decrease with mesh refinement and, at the same time, allows ρ_{\max} to mimic, to a certain degree, the time-dependent pointwise density ρ present in (20) (inversely proportional to J). Our tests indicate that this choice of α_0 is critical to obtain accurate tangential motion at the boundary as the mesh refinement.

Let $\mathbf{v} = v_{j;b}$ be an $[n_{\mathcal{V}} \times d]$ -vector,

$$\mathbf{M}_{\mathcal{V}} = \mathbf{M}_{a_i b_j} = (\rho w_a, w_b \delta_{ij})_{\Omega(t)} + \langle \alpha_0 \rho_{\max} L w_a n_i, w_b n_j \rangle_{\Gamma_0} \quad (23a)$$

be a $[(n_{\mathcal{V}} \times d) \times (n_{\mathcal{V}} \times d)]$ -square matrix with $a, b \in [1, n_{\mathcal{V}}]$ and $i, j \in [1, d]$,

$$\mathbf{F} = \mathbf{F}_{a;l} = (\sigma_{ik}, \phi_l \nabla_{x_k} w_a)_{\Omega(t)} - \langle (n_k \sigma_{kj} n_j) n_i, w_a \phi_l \rangle_{\Gamma(t)} + \langle \beta \rho c_s \mathbf{v} \cdot \mathbf{n}, w_a n_i \phi_l \rangle_{\Gamma(t)} \quad (23b)$$

be a $[(n_{\mathcal{V}} \times d) \times n_{\mathcal{E}}]$ -matrix with $1 \leq l \leq n_{\mathcal{E}}$, and

$$\mathbf{B} = \mathbf{B}_{a;l} = (\rho b_l, w_a)_{\Omega(t)} \quad (23c)$$

be a $[n_{\mathcal{V}} \times d]$ -vector. Then the semidiscrete Lagrangian momentum equation can be written in matrix vector form as

$$\mathbf{M}_{\mathcal{V}} \frac{d\mathbf{v}}{dt} = -\mathbf{F} \mathbf{1} + \mathbf{B}, \quad (24)$$

where $\mathbf{1}$ is a $[n_{\mathcal{E}}]$ -vector whose entries are all equal to one.

3.4. Semi-discrete energy conservation law

We formulate the discrete energy conservation equation by multiplying (2d) with a test function $\phi_l \in \mathcal{E}(\Omega(t))$ and integrating over the domain $\Omega(t)$

$$(\rho \dot{e}, \phi_l)_{\Omega(t)} - (\boldsymbol{\sigma} : \nabla_x \mathbf{v}, \phi_l)_{\Omega(t)} + (\nabla_x \cdot \mathbf{q} - \rho r, \phi_l)_{\Omega(t)} = 0. \quad (25)$$

To ensure conservation of total energy, we add

$$\langle \mathbf{n} \cdot (\boldsymbol{\sigma} \mathbf{n}) \mathbf{v} \cdot \mathbf{n}, \phi_l \rangle_{\Gamma(t)} - \langle \beta \rho c_s (\mathbf{v} \cdot \mathbf{n})^2, \phi_l \rangle_{\Gamma(t)}. \quad (26)$$

to the left hand side of (25). Observe that these are residual terms, since they weakly enforce the boundary condition $\mathbf{v} \cdot \mathbf{n} = 0$. Expanding the internal energy in terms of the moving thermodynamic basis and using tensor notation give us

$$\frac{de_m}{dt} (\rho \phi_m, \phi_l)_{\Omega(t)} = (\boldsymbol{\sigma} : \nabla_x \cdot \mathbf{v}, \phi_l)_{\Omega(t)} + (\rho r - \nabla_x \cdot \mathbf{q}, \phi_l)_{\Omega(t)} - \langle \mathbf{n} \cdot (\boldsymbol{\sigma} \mathbf{n}) \mathbf{v} \cdot \mathbf{n}, \phi_l \rangle_{\Gamma(t)} + \langle \beta \rho c_s (\mathbf{v} \cdot \mathbf{n})^2, \phi_l \rangle_{\Gamma(t)}. \quad (27)$$

Defining

$$\mathbf{M}_{\mathcal{E}} = \mathbf{M}_{m;l} = (\rho \phi_m, \phi_l)_{\Omega(t)} \quad (28a)$$

be a $[n_{\mathcal{E}} \times n_{\mathcal{E}}]$ -square matrix with $1 \leq m, l \leq n_{\mathcal{E}}$ and

$$\mathbf{R} = \mathbf{R}_l = (\rho r - \nabla_x \cdot \mathbf{q}, \phi_l), \quad (28b)$$

be a $[n_{\mathcal{E}}]$ -vector, the semi-discrete energy conservation can be written in matrix-vector form as

$$\mathbf{M}_{\mathcal{E}} \frac{d\mathbf{e}}{dt} = \mathbf{F}^T \mathbf{v} + \mathbf{R}, \quad (29)$$

Remark 1. The mass matrices $\mathbf{M}_{\mathcal{V}}$ and $\mathbf{M}_{\mathcal{E}}$ are independent of time due to (2b) and the fact that all the shape functions are independent of time. Namely,

$$\frac{d\mathbf{M}_{\mathcal{V}}}{dt} = \frac{d}{dt}(\rho w_a, w_b \delta_{ij})_{\Omega(t)} + \frac{d}{dt}(\alpha_0 \rho_{\max} L w_a, w_b \delta_{ij})_{\Gamma_0} = 0.$$

$$\frac{d\mathbf{M}_{\mathcal{E}}}{dt} = \frac{d}{dt}(\rho \phi_m, \phi_l)_{\Omega(t)} = 0.$$

3.5. Artificial viscosity operator

To ensure a comprehensive presentation of the proposed method, this section details the formulas associated with the artificial viscosity operator σ_{art} , which align with those in [10].

The artificial viscosity tensor σ_{art} is added to the semidiscrete equations (24) and (29) to regularize shock wave propagation.

This technique was originally introduced by Von Neumann and Richtmyer [28], whereby the discrete Euler equations are augmented with a diffusion term scaled by a special mesh dependent nonlinear coefficient μ . In particular, we add

$$(\sigma_{\text{art}}, \nabla_x \mathbf{w}_{i,a})_{\Omega(t)}$$

in the momentum equation and

$$-(\sigma_{\text{art}}, \nabla_x \mathbf{v}, \phi_l)_{\Omega(t)}$$

in the energy equation. From [10] and [21], we choose

$$\sigma_{\text{art}} = \mu_{s_1} \epsilon(\mathbf{v}) \quad (30)$$

with $\epsilon(\mathbf{v}) = \frac{1}{2}(\nabla \mathbf{v} + (\nabla \mathbf{v})^T)$ is the symmetrized velocity gradient and

$$\mu_{s_1} = \rho (q_2 l_s^2 |\Delta_s \mathbf{v}| + q_1 \psi_0 \psi_1 l_s c_s), \quad (31)$$

where q_1 and q_2 are linear and quadratic scaling coefficients chosen as 1/2 and 2 respectively, $\Delta_s \mathbf{v}$ is the directional measure of compression defined in section 6.1 of [10], $l_s = l_s(x)$ is a directional length scale defined in the direction of s evaluated at a point x defined in section 6.3 in [10], ψ_1 is a compression switch which forces the linear term to vanish at points in expansion, and ψ_0 is a vorticity switch that suppresses the linear term at points where vorticity dominates the flow:

$$\psi_1 = \begin{cases} 1 & \Delta_s \mathbf{v} < 0, \\ 0 & \Delta_s \mathbf{v} \geq 0, \end{cases} \quad \psi_0 = \frac{|\nabla \cdot \mathbf{v}|}{\|\nabla \mathbf{v}\|}. \quad (32)$$

3.6. Conservation of total linear momentum and total energy

Linear momentum is conserved by the proposed numerical approach, up to $O(h^{m+1})$, where m is the regularity index from Section 2.3. Premultiplying (24) by $\mathbf{c}_{i,a}$, where $\mathbf{c}_{i,a} = c_a \boldsymbol{\zeta}_i$ is a constant $[n_{\mathcal{V}} \times d]$ -vector and $c_a w_a = 1$, we obtain:

$$\begin{aligned} \mathbf{c}_{i,a} \cdot \left(\mathbf{M}_{\mathcal{V}} \frac{d\mathbf{v}}{dt} \right) &= -\mathbf{c}_{i,a} \cdot (\mathbf{F} \mathbf{1}) + \mathbf{c}_{i,a} \cdot \mathbf{B} \\ \frac{d}{dt} \int_{\Omega_0} \rho_0 \mathbf{v} \cdot \boldsymbol{\zeta}_i &= \int_{\Omega(t)} \rho \mathbf{b} \cdot \boldsymbol{\zeta}_i - \int_{\Gamma(t)} (n_k \sigma_{kj} n_j) (\mathbf{n} \cdot \boldsymbol{\zeta}_i) - \int_{\Gamma_0} \rho_0 \underbrace{\dot{\mathbf{v}} \cdot \mathbf{n}_0}_{O(h^{m+1})} (\mathbf{n}_0 \cdot \boldsymbol{\zeta}_i) + \int_{\Gamma(t)} \beta \rho c_s \underbrace{\mathbf{v} \cdot \mathbf{n}}_{O(h^{m+1})} (\mathbf{n} \cdot \boldsymbol{\zeta}_i) \end{aligned} \quad (33)$$

The first three terms represent the statement of balance of accelerations, internal forces and boundary forces, respectively, which is the standard statement of conservation of momentum. The last two terms represent the error due to weakly enforcing $\mathbf{v} \cdot \mathbf{n} = 0$, which scales as $O(h^{m+1})$.

Total energy is conserved exactly. Premultiplying (24) by \mathbf{v}^T and (29) by $\mathbf{1}^T$, we obtain:

$$\frac{d\mathbf{E}}{dt} := \frac{d}{dt} \left(\frac{1}{2} \mathbf{v}^T \mathbf{M}_{\mathcal{V}} \mathbf{v} + \mathbf{1}^T \mathbf{M}_{\mathcal{E}} \mathbf{e} \right) = \mathbf{v}^T \mathbf{B} + \mathbf{R},$$

where we applied Remark 1.

Remark 1. Observe that the total energy defined above converges to the exact total energy as the numerical solution converges to the exact solution, similarly to the case of strong imposition of boundary conditions. In particular, while the definition of the numerical internal energy does not seem to pose any particular problem, the definition of the numerical kinetic energy must be considered with care. In fact, the numerical kinetic energy reads

$$\frac{1}{2} \mathbf{v}^T \mathbf{M}_{\mathcal{V}} \mathbf{v} = \frac{1}{2} (\rho v_{i;b} w_b, w_a v_{i;a})_{\Omega(t)} + \frac{1}{2} \langle \alpha_0 \rho_{\max} L, (\mathbf{n}_0 \cdot \mathbf{v})^2 \rangle_{\Gamma_0}. \quad (34)$$

The second term on the right hand side goes to zero as the grid is refined or the polynomial order is increased, since the boundary condition on Γ_0 will be more and more accurately satisfied. Then the proposed definition of the numerical kinetic energy is consistent with the infinite dimensional limit.

3.7. Time integration and fully discrete approximation

So far we have focused exclusively on the spatial discretization. Now we discuss the discretization of the time derivatives in the nonlinear system of ODEs (2a), (24) and (29), obtained from the spatial discretization of the Euler equations. In this section we consider a general high-order temporal discretization method and demonstrate its impact on the semidiscrete conservations laws.

We adopt the same *modified* midpoint Runge-Kutta second-order scheme proposed in [5, 8, 10, 23]. This choice of time integrator guarantees the proposed formulation conserves total energy without resorting to any staggered approach in time. Let $t \in \{t_n\}_{n=0}^{N_t}$ and associate with each moment in time, t_n , the computational domain $\Omega^n \equiv \Omega(t_n)$. Let $\mathbf{Y} = (\mathbf{v}; \mathbf{e}; \mathbf{x})$ be the hydrodynamic state vector. We identify the quantities of interest defined on Ω^n with a superscript n , denote by Δt the time-step. The fully discrete numerical algorithm then reads

$$\begin{aligned} \mathbf{v}^{n+\frac{1}{2}} &= \mathbf{v}^n - \frac{\Delta t}{2} \mathbf{M}_{\mathcal{V}}^{-1} (\mathbf{F}^n \mathbf{1} - \mathbf{B}^n), & \mathbf{v}^{n+1} &= \mathbf{v}^n - \Delta t \mathbf{M}_{\mathcal{V}}^{-1} (\mathbf{F}^{n+\frac{1}{2}} \mathbf{1} - \mathbf{B}^{n+\frac{1}{2}}), \\ \mathbf{e}^{n+\frac{1}{2}} &= \mathbf{e}^n + \frac{\Delta t}{2} \mathbf{M}_{\mathcal{E}}^{-1} ((\mathbf{F}^n)^T \mathbf{v}^{n+\frac{1}{2}} + \mathbf{R}^n), & \mathbf{e}^{n+1} &= \mathbf{e}^n + \Delta t \mathbf{M}_{\mathcal{E}}^{-1} ((\mathbf{F}^{n+\frac{1}{2}})^T \bar{\mathbf{v}}^{n+\frac{1}{2}} + \mathbf{R}^{n+\frac{1}{2}}), \\ \mathbf{x}^{n+\frac{1}{2}} &= \mathbf{x}^n + \frac{\Delta t}{2} \mathbf{v}^{n+\frac{1}{2}}, & \mathbf{x}^{n+1} &= \mathbf{x}^n + \Delta t \bar{\mathbf{v}}^{n+\frac{1}{2}}, \end{aligned}$$

where $\mathbf{F}^k = \mathbf{F}(\mathbf{Y}^k)$ and $\bar{\mathbf{v}}^{n+\frac{1}{2}} = (\mathbf{v}^{n+1} + \mathbf{v}^n)/2$.

Proposition 1. *The RK2-average scheme described above conserves the discrete total linear momentum up to $O(h^{m+1})$.*

Proof. Let $\mathbf{c}_{i;a} = c_a \zeta_i$ is a constant $[n_{\mathcal{V}} \times d]$ -vector and $c_a w_a = 1$, then the change in linear momentum (LM) can be expressed as

$$\begin{aligned} LM^{n+1} - LM^n &= \mathbf{c}_{i;a} \cdot (\mathbf{M}_{\mathcal{V}} (\mathbf{v}^{n+1} - \mathbf{v}^n)) = -\Delta t \mathbf{c}_{i;a} \cdot (\mathbf{F}^{n+\frac{1}{2}} \mathbf{1} - \mathbf{B}^{n+\frac{1}{2}}) = \Delta t \int_{\Omega(t)^{n+\frac{1}{2}}} (\rho \mathbf{b})^{n+\frac{1}{2}} \cdot \zeta_i \\ &\quad - \Delta t \int_{\Gamma(t)^{n+\frac{1}{2}}} (n_k \sigma_{kj} n_j)^{n+\frac{1}{2}} (\mathbf{n}^{n+\frac{1}{2}} \cdot \zeta_i) \\ &\quad + \Delta t \int_{\Gamma(t)^{n+\frac{1}{2}}} \beta (\rho c_s)^{n+\frac{1}{2}} \underbrace{(\mathbf{v} \cdot \mathbf{n})^{n+\frac{1}{2}}}_{O(h^{m+1})} (\mathbf{n}^{n+\frac{1}{2}} \cdot \zeta_i) \end{aligned}$$

The first two terms on the right hand side above are the same as the ones for a strong boundary condition enforcement and the last term is the $O(h^{n+1})$ error from weakly enforcing $\mathbf{v} \cdot \mathbf{n} = 0$. \square

Proposition 2. *The RK2-average scheme described above conserves the discrete total energy exactly.*

Proof. The change in kinetic energy (KE) and internal energy (IE) can be expressed as

$$KE^{n+1} - KE^n = (\mathbf{v}^{n+1} - \mathbf{v}^n) \cdot (\mathbf{M}_{\gamma} \bar{\mathbf{v}}^{n+\frac{1}{2}}) = -\Delta t (\mathbf{F}^{n+\frac{1}{2}} \mathbf{1} - \mathbf{B}^{n+\frac{1}{2}}) \cdot \bar{\mathbf{v}}^{n+\frac{1}{2}}$$

$$IE^{n+1} - IE^n = \mathbf{1} \cdot (\mathbf{M}_{\mathcal{E}} (\mathbf{e}^{n+1} - \mathbf{e}^n)) = \Delta t \mathbf{1} \cdot ((\mathbf{F}^{n+\frac{1}{2}})^T \bar{\mathbf{v}}^{n+\frac{1}{2}} + \mathbf{R}^{n+\frac{1}{2}})$$

Thus, the change in discrete total energy $KE^{n+1} + IE^{n+1} - KE^n - IE^n = \Delta t (\mathbf{B}^{n+\frac{1}{2}} \cdot \bar{\mathbf{v}}^{n+\frac{1}{2}} + \mathbf{1} \cdot \mathbf{R}^{n+\frac{1}{2}})$ is due to the presence of body force, source and heat flux terms. If $r = 0$ and $\mathbf{b} = \mathbf{q} = 0$, we see that the discrete total energy is conserved exactly, namely: $KE^{n+1} + IE^{n+1} = KE^n + IE^n$. \square

Remark 2. The RK2-average scheme described above has similar properties to the one described in [5, 8, 10, 16, 23]. In particular, it conserves exactly also angular momentum in the limit of a large number of corrector passes [16]. The RK2-average scheme can be extended to higher orders of time integration through the work presented in [20].

4. Numerical Results

We consider the standard shock hydrodynamic benchmark of the Sedov explosion [24] in various 2D and 3D domains. In all test cases, the Sedov problem consists of an ideal gas ($\gamma = 1.4$) with a delta function source of internal energy deposited at the origin such that the total energy $E_{total} = 1$. The sudden release of the energy creates an expanding shock wave, converting the initial internal energy into kinetic energy. The delta function energy source is approximated by setting the internal energy e to zero in all degrees of freedom except at the origin where the value is chosen so that the total internal energy is 1. In all of the tests, we enforce $\mathbf{v} \cdot \mathbf{n} = 0$ on all boundaries. Note that the density plots are in logarithmic scale.

All simulations are performed in a customized version of the open-source Laghos proxy application [14], which is based on the MFEM finite element library [2].

4.1. Two-dimensional Sedov explosion in a square

We consider a $[0, 1] \times [0, 1]$ domain and a final time $t = 0.8$. In Figure 2, we show plots of the velocity and density fields in addition to the mesh deformation at the final time of $t = 0.8$ for the $Q_1 - Q_0$, $Q_2 - Q_1$, $Q_3 - Q_2$ velocity-energy pairs. As it is apparent, the weak wall boundary produce solutions that are indistinguishable from those obtained with strong enforcement which are smooth and without any unphysical oscillations. A plot of the shock front locations using a weak and strong boundary enforcement for a $Q_2 - Q_1$ discretization in Figure 3a shows that they are indistinguishable from one another. Finally, in Figure 3b we see that shock front location attained from weak boundary condition enforcement converges to the exact location with mesh refinement.

4.2. Two-dimensional Sedov explosion in a trapezoid

We perform the Sedov test in a trapezoidal domain and show in Figure 4 plots of the velocity and density fields in addition to the mesh deformation at the final time of $t = 1.3$ for the $Q_1 - Q_0$, $Q_2 - Q_1$, $Q_3 - Q_2$ velocity-energy pairs. It is worth mentioning that conducting this test with strong wall boundary enforcement is cumbersome, as it would require enforcement of linear constraints on the boundary DOFs. The weak wall boundary conditions produce the correct shock bounce-back behavior on the top boundary with solutions that remain smooth and do not show any unphysical oscillations.

4.3. Two-dimensional Sedov explosion in a square with a circular hole

We perform the Sedov test in a unit square with a circular hole and show in Figure 5 plots of the velocity and density fields in addition to the mesh deformation at the final time of $t = 0.8$ for the $Q_1 - Q_0$, $Q_2 - Q_1$, $Q_3 - Q_2$ velocity-energy pairs. It is worth mentioning that conducting this test with strong wall boundary enforcement is very cumbersome, due to the curvature of the internal surface, while it is seamless with our proposed weak form. The weak wall boundary enforcement produces the expected response and smooth solutions without any unphysical oscillations. This test demonstrates the robustness of the proposed algorithm, which allows the shock wave to propagate around the curved obstacle under extreme levels of mesh deformation, even for the $Q_3 - Q_2$ discretization.

4.4. Two-dimensional Sedov explosion in a square with a square hole

We perform the Sedov test in a unit square with a square hole rotated by 20 degrees counter-clockwise and show plots of the velocity and density fields in addition to the mesh deformation at the final time of $t = 0.8$ for the $Q_1 - Q_0$, $Q_2 - Q_1$, $Q_3 - Q_2$ velocity-energy pairs as shown in Figure 6. The weak wall boundary conditions produce the expected response and smooth solutions without any unphysical oscillations. The proposed method demonstrates its robustness by capturing the propagation of the shock wave past the sharp top left corner of the obstacle.

4.5. Two-dimensional Sedov explosion in a disc

We perform the Sedov test in a circular domain and show plots of the velocity and density fields in addition to the mesh deformation at the different points-in-time until $t = 20.0$ for $Q_2 - Q_1$ velocity-energy pair as shown in Figure 7. Observe that the shock slides correctly along the outside curved boundary without shape distortions. Similarly, the curved shape of the boundary is not affected by the strong shock bounce. The solution appears physically correct without any unphysical oscillations.

4.6. Three-dimensional Sedov explosion in a cube

We consider a $[0, 1] \times [0, 1] \times [0, 1]$ domain and a final time $t = 0.8$. In Figure 8 we show plots of the velocity and density fields in different cross-sections at $t = 0.8$ for the $Q_1 - Q_0$, $Q_2 - Q_1$, $Q_3 - Q_2$ velocity-energy pairs. The weak wall boundary conditions produce solutions indistinguishable from those obtained with strong enforcement.

4.7. Three-dimensional Sedov explosion in a cube with a spherical hole

We perform the Sedov test in a unit cube with a spherical hole and show plots of the velocity and density fields in different cross-sections at the final time of $t = 0.8$ for the $Q_1 - Q_0$, $Q_2 - Q_1$, $Q_3 - Q_2$ velocity-energy pairs as shown in Figure 5. We observe similar behavior as in the corresponding two-dimensional tests, confirming that the method is directly applicable to simulations in complex three-dimensional domains.

5. Conclusions

We developed a framework for the weak imposition of slip wall boundary conditions in Lagrangian hydrodynamics simulations. The advantage of the proposed approach was assessed in a number of computations involving domains with nontrivial and curved boundaries. Through these simulations, we demonstrated the flexibility, robustness, and accuracy of the proposed approach, and consequently its overall superiority with respect to the strong imposition of similar boundary conditions. Future work will be directed to extend these developments in the context of ALE methods, and to obtain an integrated approach to multi-material ALE/Lagrangian hydrodynamics [4]. We will also leverage the new capability in order to develop novel methods for shifted slip wall boundary conditions, a technology that will enable hydrodynamics simulations in complex domains that won't have to be meshed exactly.

Acknowledgments

The authors of Duke University are gratefully thanking the generous support of Lawrence Livermore National Laboratories, through a Laboratory Directed Research & Development (LDRD) Agreement. This work performed under the auspices of the U.S. Department of Energy by Lawrence Livermore National Laboratory under Contract DE-AC52-07NA27344, LLNL-JRNL-853773. Guglielmo Scovazzi has also been partially supported by the National Science Foundation, Division of Mathematical Sciences (DMS), under Grant 2207164.

References

- [1] Rémi Abgrall, Konstantin Lipnikov, Nathaniel Morgan, and Svetlana Tokareva. Multidimensional staggered grid residual distribution scheme for Lagrangian hydrodynamics. *SIAM J. Sci. Comp.*, 42(1):A343–A370, 2020.
- [2] R. Anderson, J. Andrej, A. Barker, J. Bramwell, J.-S. Camier, J. Cervený, V. Dobrev, Y. Dudouit, A. Fisher, Tz. Kolev, W. Pazner, M. Stowell, V. Tomov, I. Akkerman, J. Dahm, D. Medina, and S. Zampini. MFEM: A modular finite element methods library. *Computers & Mathematics with Applications*, 81:42–74, 2021.
- [3] R. Anderson, A. Black, L. Busby, R. Bleile B. Blakeley, J.-S. Camier, J. Ciurej, V. Dobrev, A. Cook, N. Elliott, J. Grondalski, R. Hornung, C. Harrison, Tz. Kolev, M. Legendre, W. Nissen, W. Liu, B. Olson, M. Osawe, O. Pearce, G. Papadimitrou, R. Pember, A. Skinner, T. Stitt, D. Stevens, L. Taylor, V. Tomov, A. Vargas, R. Rieben, K. Weiss, and D. White. The multiphysics on advanced platforms project, 2020.
- [4] Robert W. Anderson, Veselin A. Dobrev, Tzanio V. Kolev, Robert N. Rieben, and Vladimir Z. Tomov. High-order multi-material ALE hydrodynamics. *SIAM J. Sci. Comp.*, 40(1):B32–B58, 2018.
- [5] Andrew J Barlow. A compatible finite element multi-material ALE hydrodynamics algorithm. *International journal for numerical methods in fluids*, 56(8):953–964, 2008.
- [6] Marek Behr. On the application of slip boundary condition on curved boundaries. *International journal for numerical methods in fluids*, 45(1):43–51, 2004.
- [7] D. J. Benson. Computational methods in Lagrangian and Eulerian hydrocodes. *Computer Methods in Applied Mechanics and Engineering*, 99:235–394, 1992.
- [8] EJ Caramana, DE Burton, Mikhail J Shashkov, and PP Whalen. The construction of compatible hydrodynamics algorithms utilizing conservation of total energy. *Journal of Computational Physics*, 146(1):227–262, 1998.
- [9] Gautier Dakin, Bruno Després, and Stéphane Jaouen. High-order staggered schemes for compressible hydrodynamics. weak consistency and numerical validation. *SIAM J. Sci. Comp.*, 376:339–364, 2019.
- [10] V. Dobrev, Tz. Kolev, and R. Rieben. High-order curvilinear finite element methods for Lagrangian hydrodynamics. *SIAM J. Sci. Comp.*, 34(5):606–641, 2012.
- [11] MS Engelman, RL Sani, and PM Gresho. The implementation of normal and/or tangential boundary conditions in finite element codes for incompressible fluid flow. *International Journal for Numerical Methods in Fluids*, 2(3):225–238, 1982.
- [12] Elena Gaburro, Walter Boscheri, Simone Chiocchetti, Christian Klingenberg, Volker Springel, and Michael Dumbser. High order direct Arbitrary-Lagrangian-Eulerian schemes on moving Voronoi meshes with topology changes. *J. Comput. Phys.*, 407:109167, 2020.
- [13] Tzanio V. Kolev, Paul Fischer, Misun Min, Jack Dongarra, Jed Brown, Veselin Dobrev, Timothy Warburton, Stanimire Tomov, Mark Shephard, Ahmad Abdelfattah, Valeria Barra, Natalie Beams, Jean-Sylvain Camier, Noel Chalmers, Yohann Dudouit, Ali Karakus, Ian Karlin, Stefan Kerkemeier, Yu-Hsiang Lan, David Medina, Elia Merzari, Aleksandr Obabko, Will Pazner, Thilina Rathnayake, Cameron Smith, Lukas Spies, Kasia Świrydowicz, Jeremy Thompson, Ananias Tomboulides, and Vladimir Z. Tomov. Efficient exascale discretizations: High-order finite element methods. *Int. J. High Perform. Comput. Appl.*, 35(6):527–552, 2021.
- [14] Laghos: High-order Lagrangian hydrodynamics miniapp, 2023. <http://github.com/CEED/Laghos>.
- [15] Xiaodong Liu, Nathaniel R. Morgan, and Donald E. Burton. A high-order Lagrangian discontinuous Galerkin hydrodynamic method for quadratic cells using a subcell mesh stabilization scheme. *J. Comput. Phys.*, 386:110–157, 2019.
- [16] E Love and G Scovazzi. On the angular momentum conservation and incremental objectivity properties of a predictor/multi-corrector method for Lagrangian shock hydrodynamics. *Computer methods in applied mechanics and engineering*, 198(41-44):3207–3213, 2009.
- [17] R. Menikoff and B. J. Plohr. The Riemann problem for fluid flow of real materials. *Reviews of Modern Physics*, 61(1):75–130, 1989.
- [18] J. A. Nitsche. Über ein Variationsprinzip zur Lösung Dirichlet-Problemen bei Verwendung von Teilräumen, die keinen Randbedingungen unterworfen sind. *Abh. Math. Sem. Univ., Hamburg*, 36:9–15, 1971.
- [19] Aditya K. Pandare, Jacob Waltz, and Jozsef Bakosi. Multi-material hydrodynamics with algebraic sharp interface capturing. *Comput. Fluids*, 215:104804, 2021.
- [20] Adrian Sandu, Vladimir Z. Tomov, Lenka Cervena, and Tzanio V. Kolev. Conservative high-order time integration for Lagrangian hydrodynamics. *SIAM J. Sci. Comp.*, 43(1):A221–A241, 2021.
- [21] G. Scovazzi, M.A. Christon, T.J.R. Hughes, and J.N. Shadid. Stabilized shock hydrodynamics: I. a Lagrangian method. *Computer Methods in Applied Mechanics and Engineering*, 196(4):923–966, 2007.
- [22] G Scovazzi, T Song, and X Zeng. A velocity/stress mixed stabilized nodal finite element for elastodynamics: Analysis and computations with strongly and weakly enforced boundary conditions. *Computer Methods in Applied Mechanics and Engineering*, 325:532–576, 2017.
- [23] Guglielmo Scovazzi, Edward Love, and MJ Shashkov. Multi-scale Lagrangian shock hydrodynamics on Q1/P0 finite elements: Theoretical framework and two-dimensional computations. *Computer methods in applied mechanics and engineering*, 197(9-12):1056–1079, 2008.
- [24] Leonid I. Sedov. *Similarity and Dimensional Methods in Mechanics*. CRC Press, Boca Raton, FL, 10th edition, 1993.
- [25] T Song and G Scovazzi. A Nitsche method for wave propagation problems in time domain. *Computer Methods in Applied Mechanics and Engineering*, 293:481–521, 2015.

- [26] Ting Song, Alex Main, Guglielmo Scovazzi, and Mario Ricchiuto. The Shifted Boundary Method for hyperbolic systems: Embedded domain computations of linear waves and shallow water flows. Journal of Computational Physics, 369:45–79, 2018.
- [27] Arturo Vargas, Thomas M. Stitt, Kenneth Weiss, Vladimir Z. Tomov, Jean-Sylvain Camier, Tzanio Kolev, and Robert N. Rieben. Matrix-free approaches for GPU acceleration of a high-order finite element hydrodynamics application using MFEM, Umpire, and RAJA. Int. J. High Perform. Comput. Appl., 36(4):492–509, 2022.
- [28] J. Von Neumann and R. D. Richtmyer. A method for the numerical calculation of hydrodynamic shocks. Journal of Applied Physics, 21(3):232–237, March 1950.
- [29] T. Warburton and J.S. Hesthaven. On the constants in hp-finite element trace inverse inequalities. Computer Methods in Applied Mechanics and Engineering, 192:2765–2773, 2003.

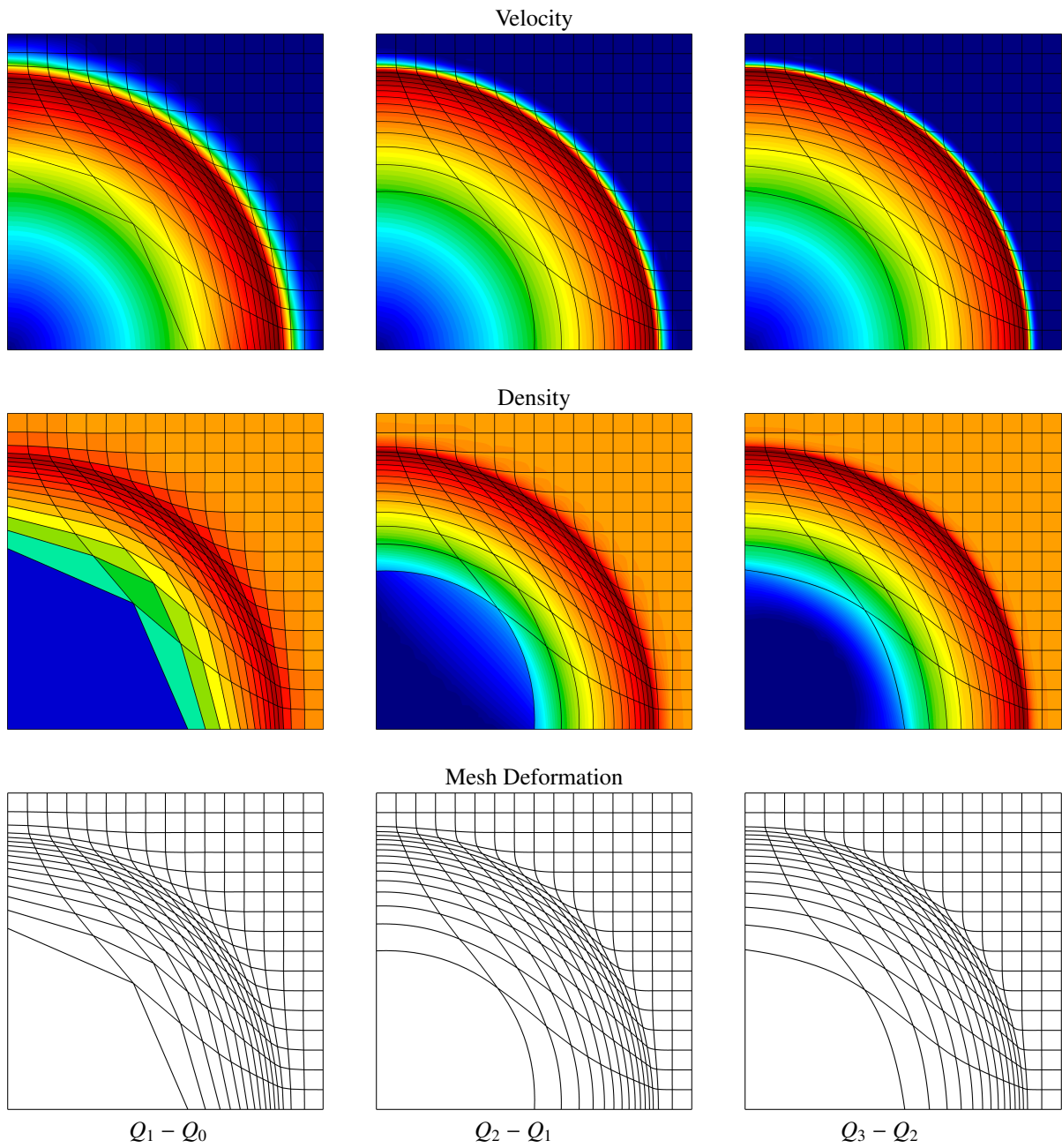
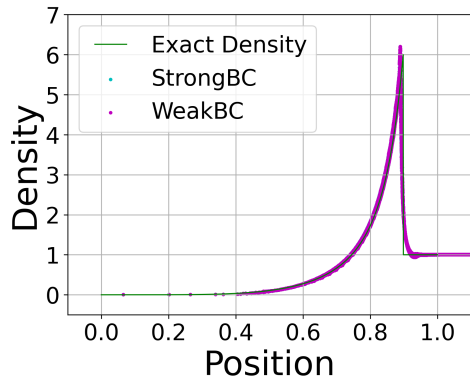
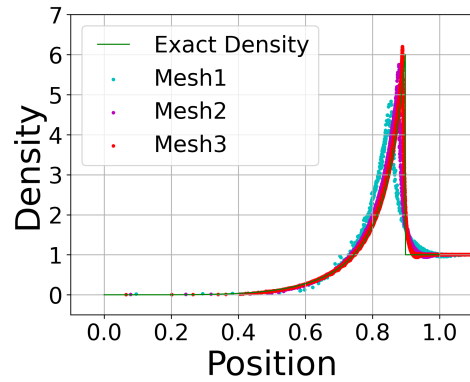


Figure 2: Plots of the velocity and density fields in addition to the mesh deformation for the planar Sedov test using $Q_1 - Q_0$, $Q_2 - Q_1$, $Q_3 - Q_2$ velocity-energy pairs.



(a) Comparison between the shock front position between strong and weak boundary enforcement with the exact solution.



(b) Convergence study for the shock front with weak boundary condition enforcement.

Figure 3: Plots comparing the shock front between strong and weak boundary condition enforcement (left) and a convergence study for weak boundary condition enforcement (right) for a Q2-Q1 velocity-energy pair.

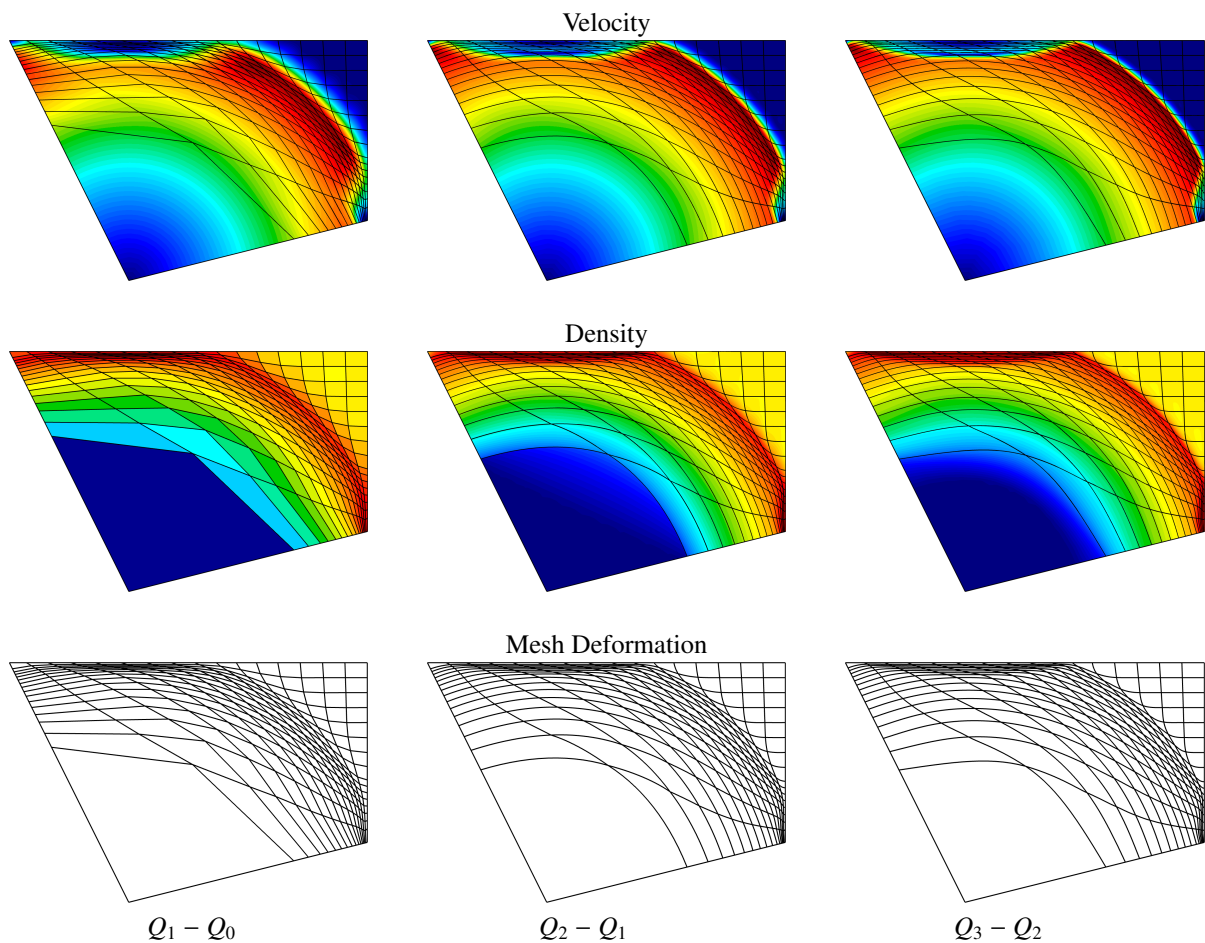


Figure 4: Plots of the velocity and density fields in addition to the mesh deformation for the Sedov test in a trapezoidal domain using $Q_1 - Q_0$, $Q_2 - Q_1$, $Q_3 - Q_2$ velocity-energy pairs.

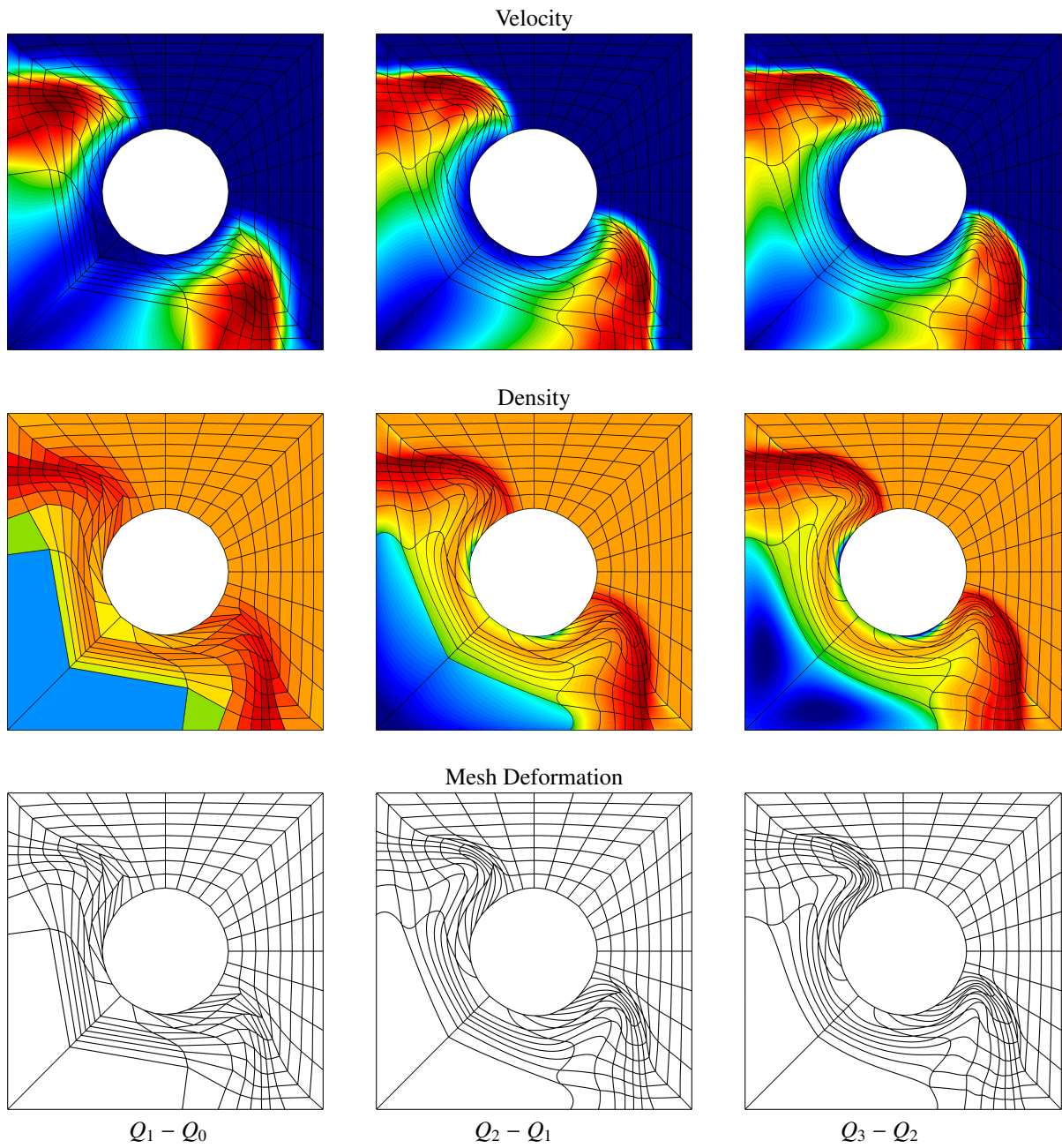


Figure 5: Plots of the velocity and density fields in addition to the mesh deformation for the Sedov test in a square domain with a circular hole using the $Q_1 - Q_0$, $Q_2 - Q_1$, $Q_3 - Q_2$ velocity-energy pairs.

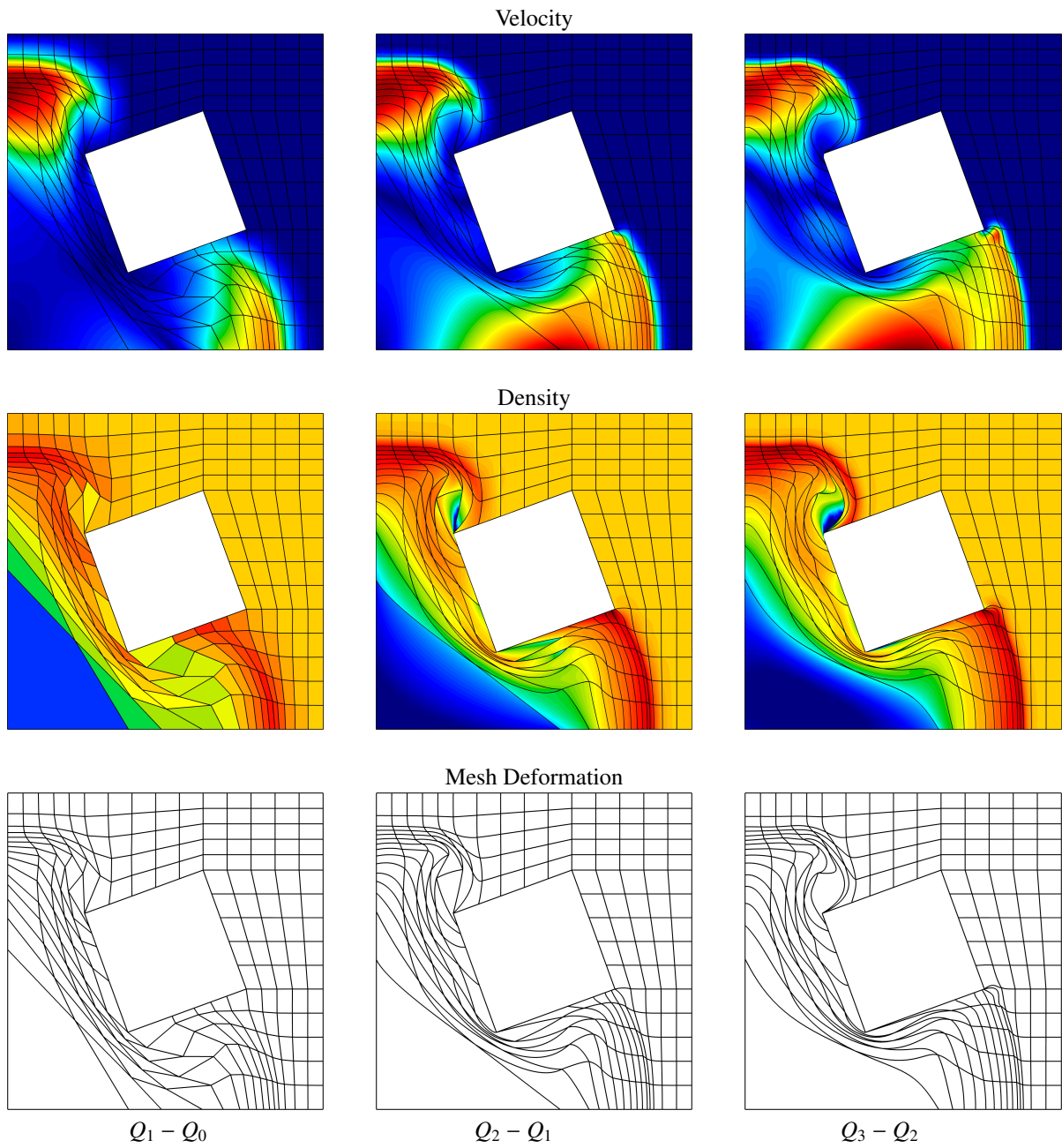


Figure 6: Plots of the velocity and density fields in addition to the mesh deformation for the Sedov test in a square domain with a square hole using the $Q_1 - Q_0$, $Q_2 - Q_1$, $Q_3 - Q_2$ velocity-energy pairs.

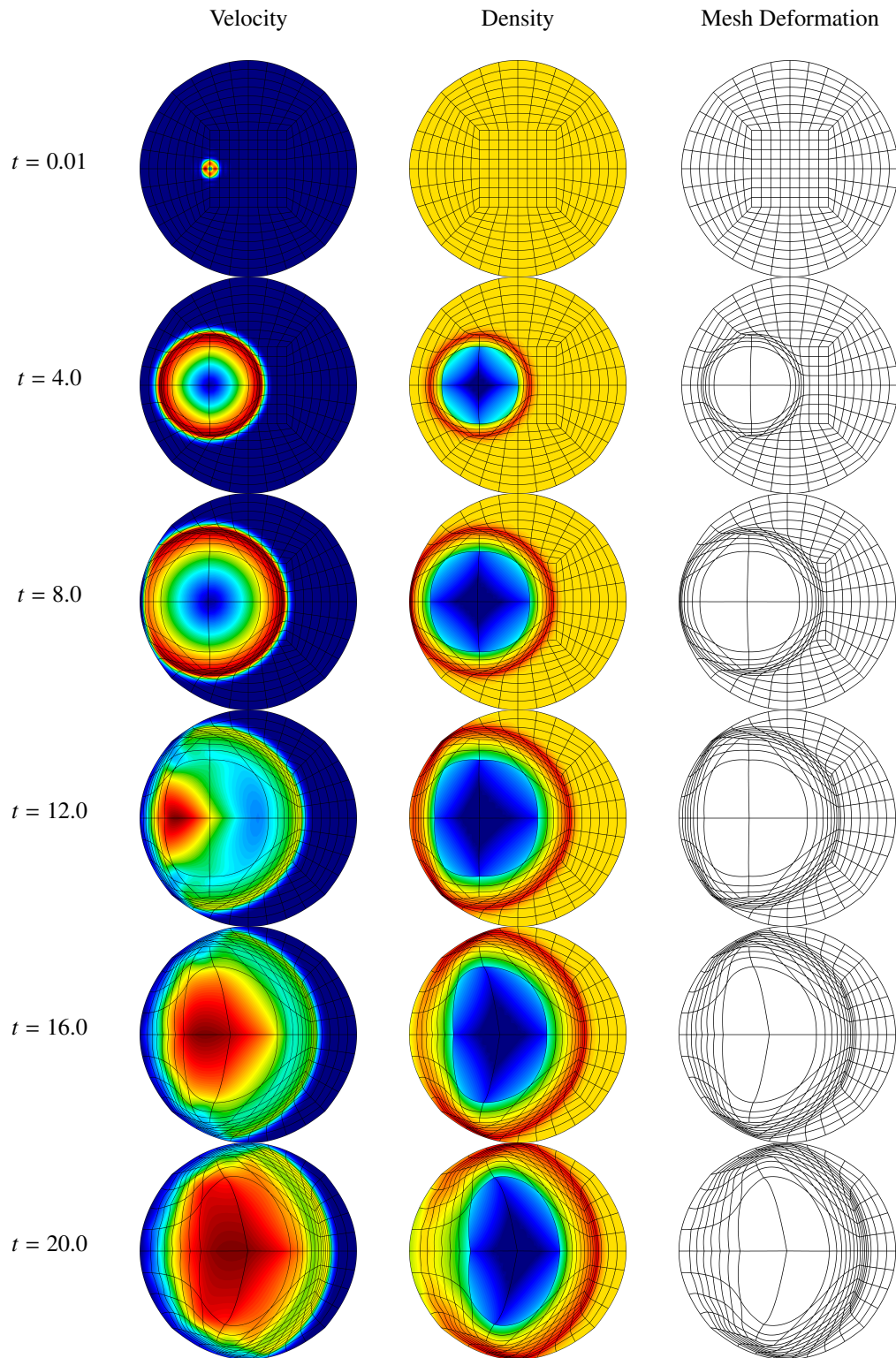


Figure 7: Plots of the velocity and density fields in addition to the mesh deformation for the Sedov test in a circular domain using a $Q_2 - Q_1$ velocity-energy pair.

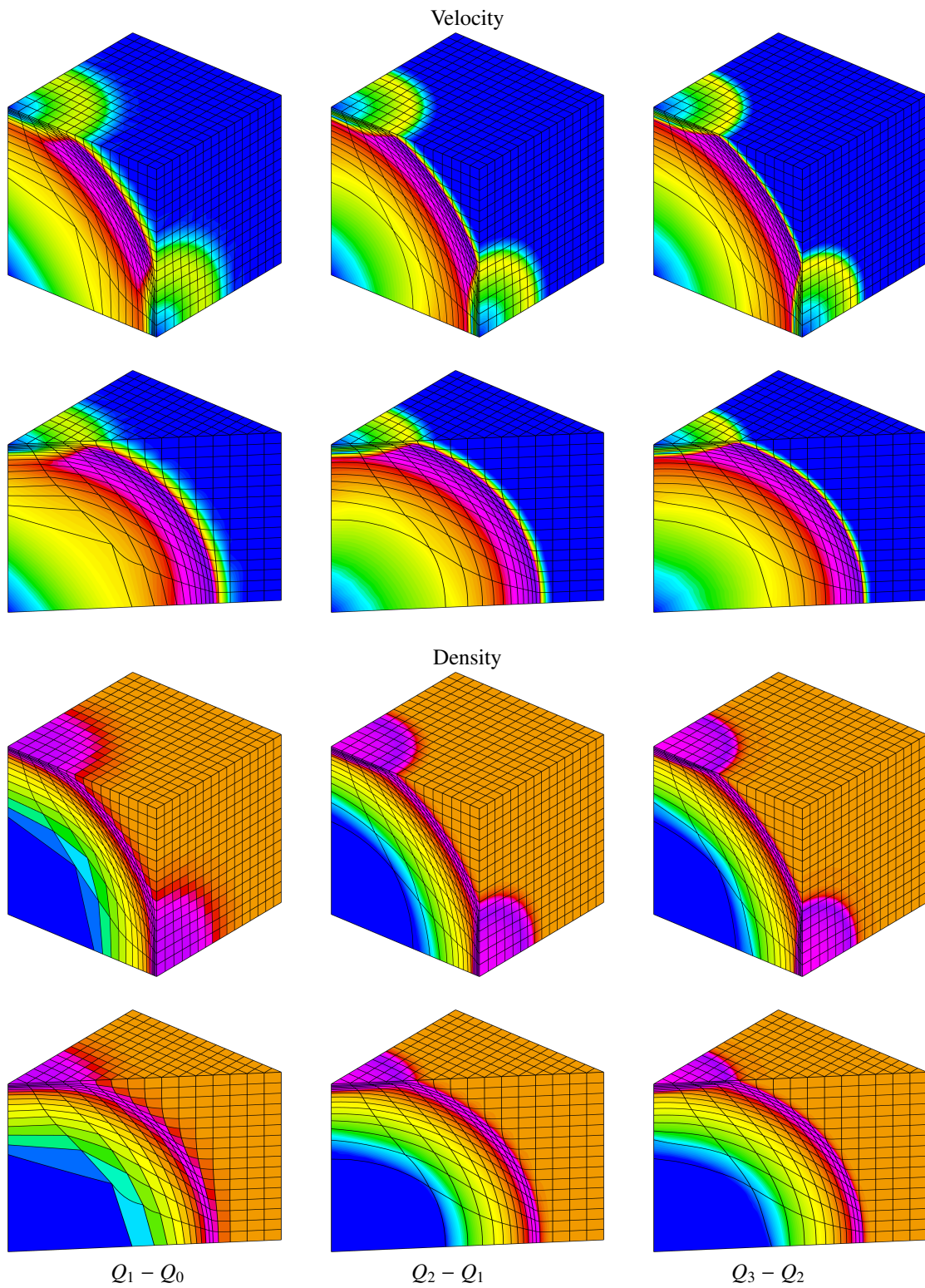


Figure 8: Plots of the velocity and density fields in addition to the mesh deformation for the three-dimensional Sedov test using $Q_1 - Q_0$, $Q_2 - Q_1$, $Q_3 - Q_2$ velocity-energy pairs. Various viewpoints and cuts are presented.

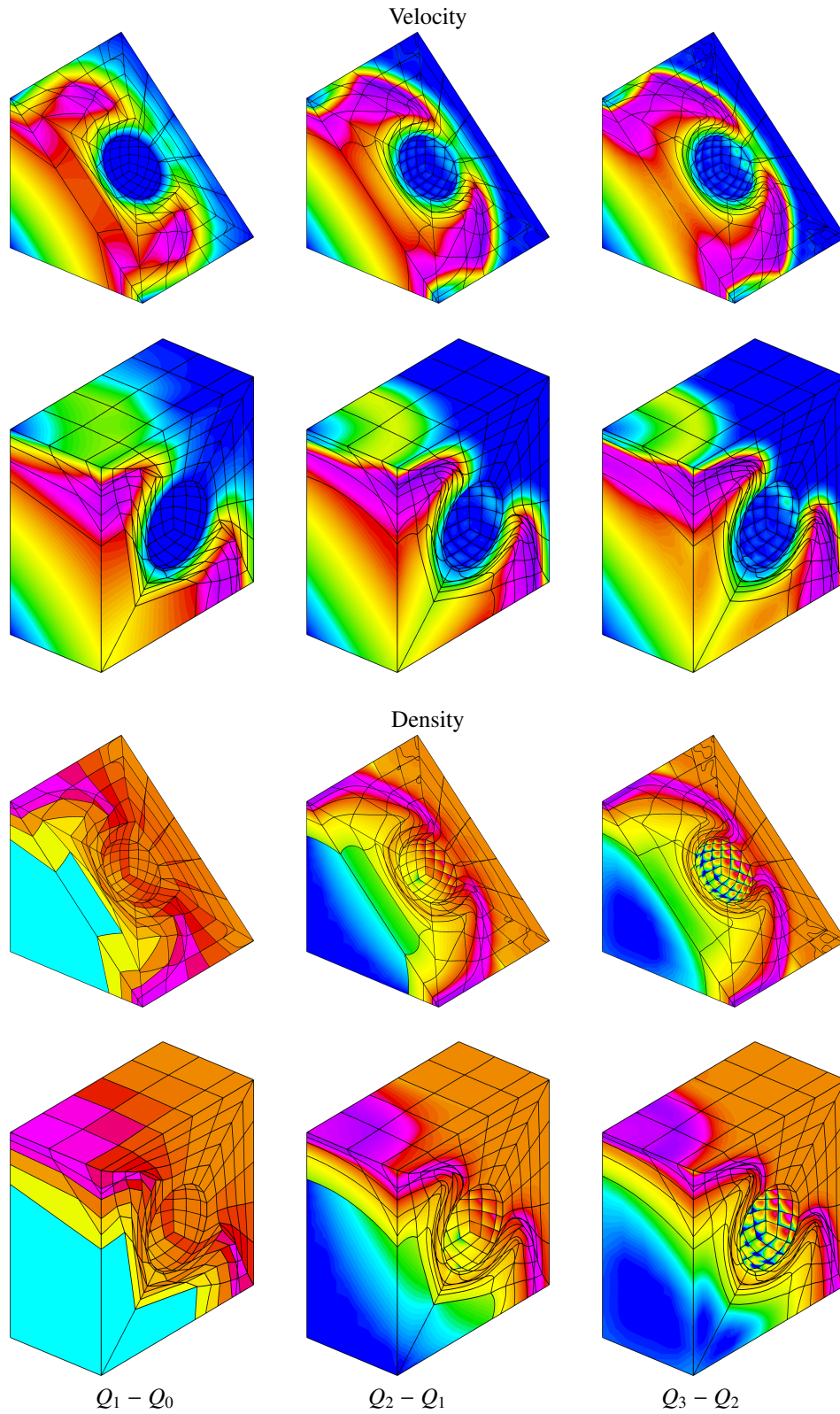


Figure 9: Plots of the velocity and density fields in addition to the mesh deformation for the planar Sedov test using $Q_1 - Q_0$, $Q_2 - Q_1$, $Q_3 - Q_2$ velocity-energy pairs. Various viewpoints and cuts are presented.